Long-term Prediction of the Gulf Stream Meander Using OceanNet: a Principled Neural Operator-based Digital Twin

Michael Gray[1], Ashesh Chattopadhyay[2], Tianning Wu[1], Anna Lowe[1], and Ruoying He[1]

[1]North Carolina State University, Raleigh, North Carolina, 27695, United States
[2]University of California- Santa Cruz, Santa Cruz, California, 95060, United States

Correspondence: Michael Gray (magray@ncsu.edu)

Abstract. Many meteorological and oceanographic processes throughout the eastern United States and western Atlantic Ocean, such as storm tracks and shelf water transport, are influenced by the position and warm sea surface temperature of the Gulf Stream (GS)- the region's western boundary current. Due to highly nonlinear processes associated with the GS, predicting its meanders and frontal position have been long-standing challenges within the numerical modeling community. While the weather and climate modeling communities have begun to turn to data-driven machine learning frameworks to overcome analogous challenges, there has been less exploration of such models in oceanography. Using a new dataset from a high-resolution data-assimilative ocean reanalysis (1993-2022) for the Northwest Atlantic Ocean, OceanNet (a neural operator-based digital twin for regional oceans) was trained to predict the GS's frontal position over subseasonal-to-seasonal timescales. Here we present the architecture of OceanNet and the advantages it holds over other machine learning frameworks explored during development while demonstrating predictions of the Gulf Stream Meander are physically reasonable over at least a 60-day period and remain stable for longer. OceanNet can generate a 120-day forecast of the Gulf Stream Meander within seconds, offering significant computational efficiency.

1 Introduction

1.1 Background: The Gulf Stream Meander

The Gulf Stream (GS) is part of the Atlantic Ocean's Western Boundary Current. Easily identifiable by sea surface height (SSH) contours (Fig. 1), the GS carries warm equatorial water northward to the mid-to-high latitudes. The GS can be divided into two frequently studied segments: the Loop Current, which flows into and out of the Gulf of Mexico, and the Gulf Stream Meander (GSM), which extends to the east once the GS passes Cape Hatteras, North Carolina (Fig. 1). Due to its vast spatial coverage and anomalously warm temperatures, the GS influences much of the weather along the eastern coast of the United States as well as Western Europe (Minobe et al., 2008). Given its importance, there has been significant effort among modelers to forecast the position of the GS across various timescales.

Robinson et al. (1988) attempted to model a 26-day period of the "GSM and Ring region" using feature modeling techniques derived from remote sensing data and the Harvard Quasi-Geostrophic Open Boundary model. The authors carried out multiple experiments across durations, GSM positions, and combinations of sea surface temperature, topography, and boundary condi-
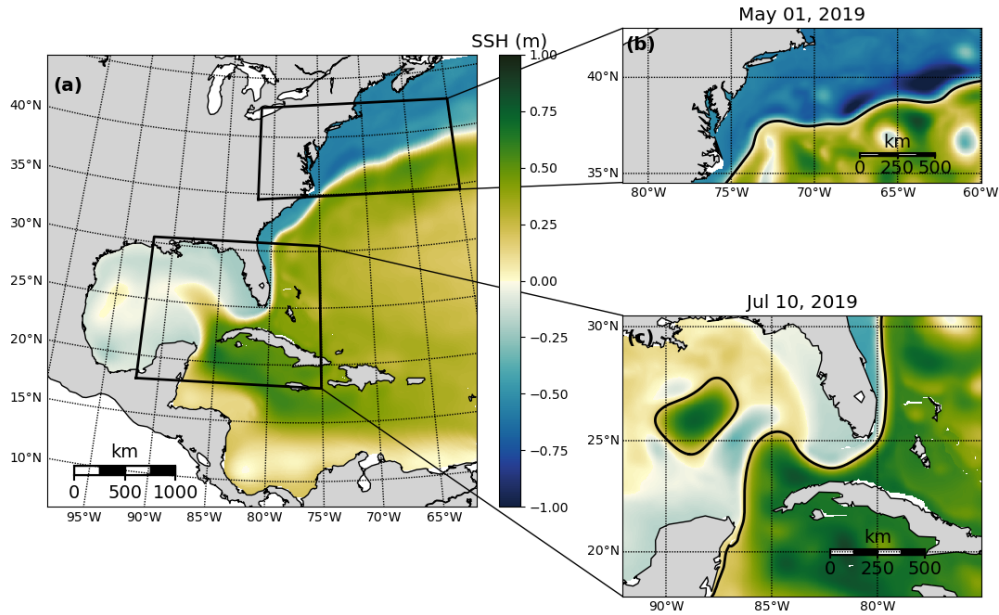
Figure 1. (a) The domain for the reanalysis data covering the northwestern Atlantic. The two subdomains used to develop OceanNet, specifically (b) the GS separation point and GSM from the central US east coast to 60°W and (c) the Loop Current eddy-shedding region in the eastern Gulf of Mexico, extending from 92°W into the Atlantic 75°W (not explored in this study). The mean SSH from from 1993-2020 in the reanalysis data is shown in (a), while (b) and (c) depict daily mean SSH on May 1, 2019, and July 10, 2019, respectively. All three domains share the same color scale.

25 tions being present. The following features were determined to be imperative to correctly simulate and achieve a convincing GSM and Ring region: ring (eddy) formation via GSM breakoffs, ring coalescence with the GSM, and ring-ring mergers, interactions, and contacts. Chen et al. (2014) modeled a case study of one particular eddy: a warm core eddy event that lasted 27 days, detached and reattached the to GSM, and influenced heat and salt fluxes on the order of 6-9 times larger than mean values. While the authors do mention this was likely the largest and most energetic event in decades, visual inspection of sea

30 surface variable plots (temperature, height, currents, etc) demonstrates how mesoscale eddy structures are frequently present around the GSM. These structures, as seen in Chen et al. (2014), can greatly influence the overall circulation and fluxes of state variables.

It has been a challenging task for numerical models to robustly simulate and predict GS dynamics, especially its separation point off Cape Hatteras, North Carolina as well as mesoscale activity along the GSM (Chassignet and Marshall, 2008). A

35 horizontal resolution of at least 1/10th degree is necessary to achieve a realistic separation point (Chassignet and Marshall, 2008). Higher resolutions are needed to properly represent the variabilities in GSM, including GS meanders and eddies, and the zonal penetration of the GS (Chassignet and Xu, 2017).

Since GSM simulations are the result of interactions on relatively small scales that propagate to much larger processes, numerical models must be carefully calibrated and include high-resolution physics. The open boundary to the east of the 40 GS exacerbates these challenges by requiring larger domains to properly capture meridional fluxes into the system. These compounding factors result in the need for massive compute power, time, and funding for numerical modelers. Conversely, machine learning predictions require a fraction of the resources; while these models may be slow to train, taking hours or even days, they result in extremely fast, cheap models that can exponentially reduce compute times and cost without making sacrifices in terms of resolution.

45 ## 1.2   Machine Learning in Marine Sciences

In the weather and climate modeling communities, data-driven machine learning methods have become a popular field of exploration and have delivered promising results in the prediction of complex atmospheric circulation (Pathak et al., 2022; Bi et al., 2023b; Lam et al., 2023). Such models have demonstrated the aforementioned advantages of machine learning while outperforming state of the art numerical weather models for lead times of 8-10 days (Pathak et al., 2022; Bi et al., 2023b; Lam 50 et al., 2023). A significant limitation of these models arises when they are integrated over longer time scales (two weeks or longer), leading to instability and the emergence of nonphysical features (see Chattopadhyay and Hassanzadeh, 2023, Fig. 1)). The cause of this instability was identified as "spectral bias", an inductive bias in all deep neural networks that hinders their ability to capture small-scale features in turbulent flows. Chattopadhyay and Hassanzadeh (2023) proposed a potential solution in the form of a framework to construct long-term stable digital twins for atmospheric dynamics. That is not to say numerical 55 weather models have a prediction horizon much longer (if at all) than two weeks, but the fact that machine learning atmospheric models are as accurate as they are on a global scale for any lead time- even if they grow unstable- is a tremendous feat. While these advances are proving fruitful for the atmospheric sciences, there has yet to be progress of equivalent magnitude in predicting physical systems in marine sciences.

Efforts in emulating ocean dynamics with deep learning-based approaches have primarily focused on predicting large-scale 60 circulation features such as those resolved by empirical orthogonal functions (EOFs) or on constructing low-dimensional representations (Wang et al., 2019; Agarwal et al., 2021). Zeng et al. (2015) demonstrated the ability to predict SSH fields in the Gulf of Mexico associated with the Loop Current with about a four week lead time (up to six weeks in some cases) based on principle component time series of satellite-observed SSH fields. Zeng et al. (2015) later became the basis of Wang et al. (2019), where, after decomposing SSH fields in the Gulf of Mexico into principle component time series, the authors 65 used a recurrent neural network, the Long Short Term Memory model (LSTM), to make a temporally-informed prediction. This method achieved valuable results, showing improved prediction accuracy of SSH fields in the Gulf of Mexico for up to 12 weeks compared to persistence, which was used as the baseline. While Zeng et al. (2015) and Wang et al. (2019) are both impressive, they share a similar problem of neglecting small-scale interactions that are important to the propagation of larger

scale features such as the separation of a loop current eddy from the Loop Current. These studies are certainly a step in the right direction, but there is ample need for more data-driven ocean models (e.g., Wang et al. (2024)) similar to the data-driven global weather models seen in Pathak et al. (2022), Bi et al. (2023b), and Lam et al. (2023)

In an attempt to advance the progress of machine learning in marine sciences, examined here is the development and performance of a neural operator-based digital twin for the northwest Atlantic Ocean's western boundary current, named OceanNet, built upon the same principles as the FouRKS model introduced in Chattopadhyay and Hassanzadeh (2023). OceanNet relies on a Fourier neural operator (FNO), which incorporates a predictor-evaluate-corrector (PEC) integration scheme to suppress autoregressive error growth. Additionally, a spectral regularizer is employed to mitigate spectral bias at small scales. OceanNet is trained on historical SSH data from a high-resolution northwest Atlantic Ocean reanalysis and demonstrates remarkable stability and competitive skills. OceanNet, on average, outperforms SSH predictions made by the state-of-the-art Regional Ocean Modeling System (ROMS) across a 120-day period while maintaining a computational cost that is 4,000,000x cheaper (ROMS:10 hours across 144 CPUs; OceanNet: 1.18 seconds on a single NVIDIA A100 GPU) following a training period of approximately 12 hours (on an NVIDIA A100 GPU with 40GB of memory).

This paper focuses on comparing variations of OceanNet and the arrival at the best architecture. For an in-depth discussion of the physical and mathematical theory behind OceanNet and each of its components, see Chttopadhyay et al. (2023). For an investigation into the performance of OceanNet in the Gulf of Mexico, a highly-dynamic region with multiple mesoscale features, with a focus on the physical processes observed in the region, see Lowe et al. (2024).

2 Data & Methods

2.1 Northwest Atlantic Ocean Reanalysis

A high-resolution northwest Atlantic regional ocean reanalysis dataset was utilized to train OceanNet (Fig. 1)(He et al.; Wu and He). This reanalysis was generated using ROMS with the ensemble Kalman filter data assimilation method (EnKFDA). Unlike the 4D-var method, the EnKFDA method does not rely on future timestep observations or require forward and adjoint model iterations during data assimilation. This approach enables the efficient creation of a data-assimilative ocean reanalysis, allowing OceanNet to be trained on a time-space continuous reanalysis dataset. The dataset features a horizontal resolution of 1/25th degree with 50 vertical layers. For surface atmospheric forcing, data from the European Center for Medium-Range Weather Forecasting Reanalysis v5 (ERA5) was employed while open boundary conditions were derived from the Copernicus Global Ocean Physics Reanalysis (GLORYS). Ten major tidal constituents from the Oregon State University TPXO tide database were used. The model incorporated 120 river inputs, sourced from the National Water Model and climatological datasets. The temporal scope of the reanalysis data used spans from January 1, 1993 to December 31, 2020, with daily averaged output. The assimilated observations encompass a variety of sources, including AVHRR and MODIS Terra sea surface temperature, AVISO along-track sea surface height anomaly, glider temperature and salinity observations from the Integrated Ocean Observing System (IOOS), and the EN4 dataset which aggregates data from Argo floats, shipboard surveys, drifters, moorings, and other sources.

2.2 Model development

A summary of model configurations discussed in the following sections can be found in Table 1 in Sect. 3.

2.3 Deep Learning Ocean Prediction

One of the groundbreaking machine learning models for weather prediction was introduced by Weyn et al. (2019), called the Deep Learning Weather Prediction (DLWP) model, and claimed the ability to predict 500-hPa geopotential height at forecast lead times of up to three days and can "...easily outperform persistence, climatology, and the dynamics-based isotropic vorticity model, but not beat an operational full-physics weather prediction model". Furthermore, Weyn et al. (2019) showed their DLWP model can output realistic atmosperic states for up to 14 days. The capabilities of the DLWP made it an attractive starting point for modeling the SSH field in regional oceans, and thus became the first iteration of OceanNet- henceforth referred as the Deep Learning Ocean Prediction model (DLOP).

DLOP is a relatively simple U-NET and overall simpler than DLWP, but the core idea is the same: pixel-wise connections of two-dimensional fields of physical variables between timesteps are sufficient to predict the evolution of such fields through time. The training of DLOP consisted of passing randomly shuffled two-dimensional SSH images from the reanalysis dataset from years 1993 through 2018 with a simple constraint of mean squared error of the predicted two-dimensional SSH field. Due to the slower evolution of ocean states than that of the 500-hPa fields used in DLWP, a lead time of four days was used for training. The SSH fields were resampled to five-day running mean fields to remove the high-frequency noise associated with SSH such as tidal variations. If $X(t)$ is the initial five-day mean field of SSH at timestep t, then $X(t + \Delta t) = \text{DLOP}(X(t))$, where Δt was determined during training to be four days. The specifics of training of DLOP are almost identical to the final training of OceanNet- explained more thoroughly in Sect. 2.5.

Once trained, DLOP was used to autoregressively predict SSH fields out to 120 days. Initially, predictions from DLOP appeared to be performing somewhat well- Root-Mean-Squared Error (RMSE) and Correlation Coefficients (CC) for a four or eight day prediction were on-par or better than other predictive models (timeseries of metrics for models discussed here can be found in Sect. 3); however, predictions using DLOP tended to a mean state within a couple of timesteps before eventually growing completely unstable and thus nonphysical (Fig. 2). A thorough investigation of DLOP led to a similar conclusion to that of Chattopadhyay and Hassanzadeh (2023); the shortcomings of the DLOP's U-NET backbone reside in its inability to capture small-scale features in turbulent flows evident by the mismatch of high wavenumbers present in the fields.

Efforts were made to try and combat this documented phenomenon, specifically those prescribed by Chattopadhyay and Hassanzadeh (2023) known as the FouRKS framework. The FouRKS framework consists of employing numerical integration (Sect. 2.4.2) and spectral regularization (Sect. 2.5.1) techniques to suppress autoregressive error growth and encourage the model's attention to correctly predict the smaller scale features present. The inclusion of numerical integration in the model architecture did improve the stability horizon of the model and thus led to much lower metric values of RMSE and CC over the 120 day prediction period, but an investigation into the actual images being produced by the model showed that DLOP was slowly tending to what can only be described as a background state of the GSM. While the numerical integration techniques
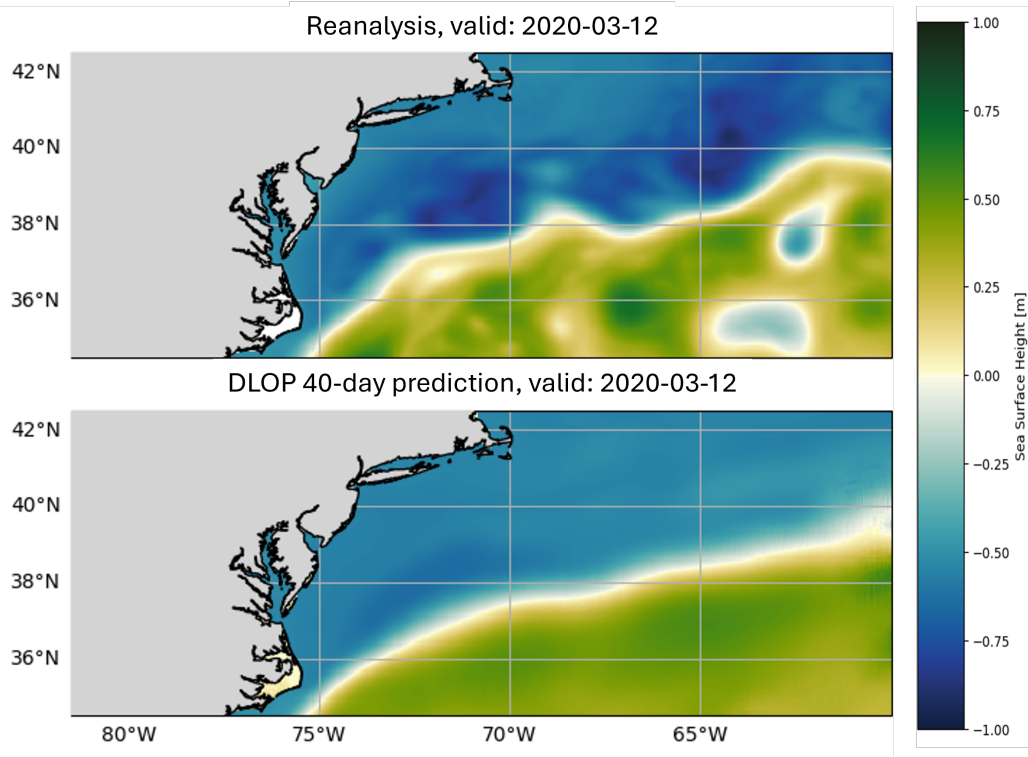
Figure 2. Prediction performance of a DLOP on the GSM region at 40 days. (Top) The SSH field from the reanalysis dataset 40 days after DLOP's initialization. Corresponds to (Bottom) The SSH field of DLOP's 40th day of prediction, demonstrating the model tending to the background state of the GSM.

helped to some degree, the spectrum of the model was still an inaccuracy of interest that could potentially be fixed when paired with the spectral regularizer. Unfortunately, both with and without the presence of the numerical integrator, the spectral regularizer caused DLOP to become even more unstable than before, as can be seen from the metrics alone- after two timesteps, the model loses all physicality and immediately propagates noise throughout the domain.

The failures of DLOP quickly evolved into a complicated problem. Despite the documentation for what was being seen by Chattopadhyay and Hassanzadeh (2023), a stable and accurate U-Net for ocean prediction could not be achieved. In numerical modeling, the suppression of error can typically be handled by integrating on shorter time scales or by adding constraints to the system to discourage the development of instability. For DLOP, integrating on shorter time scales would mean predicting with a smaller lead time each time step, which was attempted. Though the results are not shown here, extensive trial and error revealed that integrating on lead times less than four days led to DLOP not propagating anything forward- in other words, the evolution of the SSH field over three days or fewer is so small, the training process resulted in DLOP determining it would achieve the lowest error if it kept the field completely static with every prediction. This may not be a problem with atmospheric

prediction, as in DLWP, because the evolution of the atmosphere is noticeable over much shorter timescales. As for constraining the system to suppress error, this was the intent of the spectral regularization techniques but no improvement was observed.

2.4 OceanNet

150 Given the analysis of the DLOP results is consistent with previous literature (see Sect. 2.3) and that there was a noticeable improvement in the stability of DLOP with the inclusion of the numerical integrator, the techniques seen in Chattopadhyay and Hassanzadeh (2023) continued to be employed. While the spectral regularization scheme did not provide much (if any) improvement to DLOP, the idea of constraining the system's distribution of wavenumbers and stabilizing autoregressive prediction remained attractive; however, instead of using the typical two-dimensional convolutions with a U-Net structure, Fourier

155 Neural Operators (FNOs) with a multi-timestep loss function were thought to provide similar behavior. This section provides more information regarding FNOs and numerical integration while Sect. 2.5 further explains the spectral regularization and the multi-timestep constraints used in the final version of OceanNet.

2.4.1 Fourier Neural Operator (FNO)

OceanNet is built upon the FNO (Li et al., 2020). FNOs behave in a similar manner to typical two-dimensional convolutions

160 in a U-NET, but in Fourier space: a Fourier transform is performed on the input data, the highest Fourier modes are reduced to zero, then an inverse Fourier transform brings the data back to a real space where it is concatenated with the input image (Fig.3a). FNOs were introduced in Li et al. (2020) where the authors demonstrate higher performance benchmarks in terms of speed and error than any other deep learning technique to date when modeling complex fluid flow problems such as the Burger's Equation, Darcy Flow, and the Navier-Stokes equations. Due to performing operations in Fourier space, the FNO is considered

165 to be resolution agnostic- which is an advancement in and of itself since prior methods of deep learning for image-to-image translation required consistent use of the training data's resolution. The speed of FNOs comes from the various advancements in the computer science fields which have led to extremely efficient implementations of the Fast Fourier Transform; furthermore, FNOs do not rely on scanning the information in two-dimensional space as convolution and pooling layers do and instead are integrating the whole field at once.

170 As with DLOP, training utilizes labeled pairs of historical five-day-running mean SSH data in the GSM, $\mathbf{X}(t)$ (image), $\mathbf{X}(t+\Delta t)$ (label), and $\mathbf{X}(t+2\Delta t)$ (label), where $\Delta t = 4$ days. The training assumes the governing partial differential equation for the reduced ocean system involves ocean states $\mathbf{X}(t)$:

$$\frac{d\mathbf{X}(t)}{dt} = \mathbf{F}\left(\mathbf{X}\left(t\right)\right). \tag{1}$$

To integrate the system from the initial condition, $\mathbf{X}(t)$, Eq. (1) is represented in its discrete form:
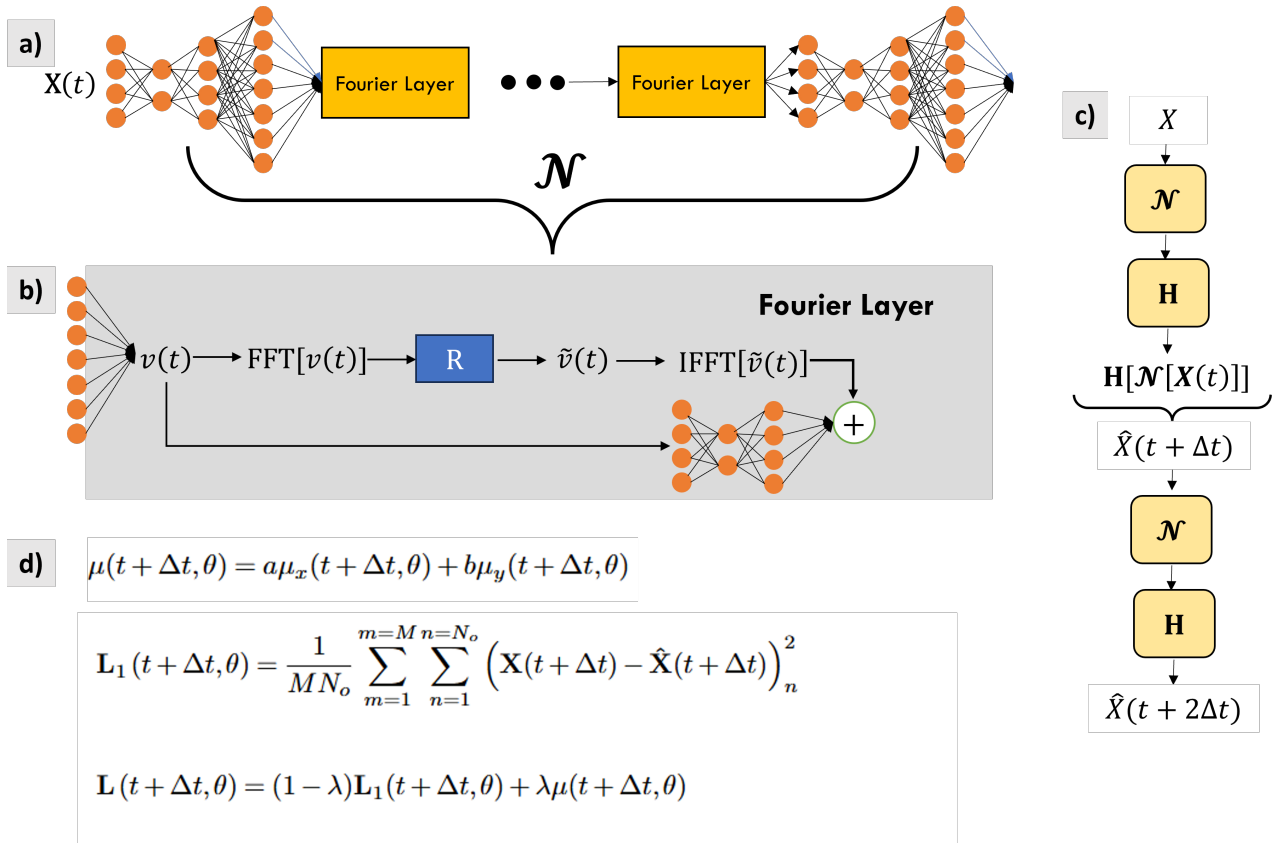
Figure 3. (a) A schematic of the OceanNet model with input image $\mathbf{X}(t)$. (b) The Fourier Neural Operator, depicted as $\mathcal{N}$ where $\nu(t)$ represents some two-dimensional field. (c) two-time-step training scheme with numerical integrator $\mathbf{H}$. (d) The loss function used, constructed by the spectral regularizer μ and MSE $\mathbf{L}_1$ for M samples to give the generalized multi-time-step function $\mathbf{L}$. The loss function is discussed in Sect. 2.5.1

175 $$\hat{\mathbf{X}}(t+\Delta t) = \mathbf{X}(t) + \underbrace{\int_{t}^{t+\Delta t} \underbrace{\mathbf{F}\left(\mathbf{X}(t)\right)}_{\mathcal{N}[\circ,\theta]} dt}_{\mathbf{H}[\circ]} .$$ (2)

Here, $\hat{\mathbf{X}}(t+\Delta t)$ is the new SSH field resulting from a single predictive step. $\mathcal{N}[\circ,\theta]$ is the neural network which will parameterize $\mathbf{F}$ with four Fourier layers, similar to Li et al. (Li et al., 2020), each layer retaining 64 Fourier modes. θ represents the $\approx 80 \times 10^6$ trainable parameters of the FNO. $\mathbf{H}[\circ]$ will represent some implicit integration scheme, e.g. the final version of OceanNet uses a higher-order predictor–evaluate–corrector (PEC) integrator (Sect. 2.4.2).

$$\rightarrow \hat{\mathbf{X}}(t + \Delta t) = \mathbf{H}[\mathcal{N}[\mathbf{X}(t), \theta]] \tag{3}$$

In other words, the predicted SSH field over a single timestep ($\hat{\mathbf{X}}(t + \Delta t)$) is approximated by integrating the neural network $\mathcal{N}[\mathbf{X}(t)]$ via the numerical integration scheme $\mathbf{H}$.

2.4.2 Predictor-Evaluate-Corrector (PEC) Integration Scheme

Similar to the higher-order integration scheme in the form of fourth-order Runge-Kutta (RK4) used in Chattopadhyay and Hassanzadeh (2023), the PEC scheme is implemented in OceanNet, represented by the operator, $\mathbf{H}[\circ]$. The operations in $\mathbf{H}$ are given by:

$$\mathcal{N}_1 = \mathcal{N}[\mathbf{X}(t), \theta], \tag{4a}$$

$$\hat{\mathbf{X}}(t + \Delta t) = \mathbf{H}[\mathcal{N}[\mathbf{X}(t), \theta]] = \mathbf{X}(t) + \mathcal{N}\left[\mathbf{X}(t) + \frac{1}{2}\mathcal{N}_1, \theta\right]. \tag{4b}$$

where $\mathcal{N}_1$ represents the operations of the neural network prior to being numerically integrated. The final predicted state is given by $\mathbf{H}[\mathcal{N}[\mathbf{X}(t), \theta]]$. Recall that $\mathcal{N}$ is our neural network and $\mathbf{H}$ is the operator performing the numerical integration.

Although most of the higher-order integration schemes, including RK4, demonstrate good performance for this problem, PEC has been identified as the most effective choice due to its compromise between higher-order integration and memory consumption during training. A theoretical study of the effect of each integration scheme on the inductive bias of the trained $\mathcal{N}$ is an active area of research, especially for understanding the role it plays on the subsequent spectral bias (Krishnapriyan et al., 2022).

2.5 Training and Validation

OceanNet for the GSM was trained on five-day running mean SSH reanalysis fields from 1993 to 2018, which helped remove high-frequency features like tides. The years 2019 and 2020 were reserved for validation and testing. All data used for training, validation, and testing underwent the same five-day running mean procedure. Before training, all of the data was randomly shuffled. There are two general steps to training OceanNet: single-timestep training and multi-timestep training. Prior to either training segment, the SSH data is normalized by removing the pixelwise 30-year mean and dividing by the pixelwise 30-year standard deviation. After normalization, the input images are fed into the model where a four day lead prediction is given. For single-timestep training, the prediction and the reanalysis image of the corresponding day are evaluated by the loss function (described in Sect. 2.5.1). For multi-timestep training, the output of the model is fed back through the model to produce an eight day lead prediction which is then evaluated by the two-timestep loss function. Based on hyper-parameter optimization via the Optuna python package, the optimal training workflow included 180 epochs of single-timestep training followed by 180 epochs of multi-timestep training. Two values were used to validate OceanNet's performance: the Modified Hausdorff Distance (explained in Sect. 3) and the value of the loss function.

2.5.1 Spectral Regularization in Fourier Space and the 2-timestep Loss Function

In OceanNet's loss function, spectral regularization was incorporated based on Fourier transforms, introduced in Chattopadhyay and Hassanzadeh (2023). This is in addition to the standard mean squared error loss (MSE) function, which is computed exclusively for grid points located over the ocean.

The spectral regularizer penalizes deviations in the Fourier modes present in the SSH field at small wavenumbers. Such deviations arise due to spectral bias, which represents an inherent inductive bias in deep neural networks (Xu et al., 2019; Chattopadhyay and Hassanzadeh, 2023). This bias is responsible for their limitations in learning the fine-scale dynamics of turbulent flow. This regularization was carried out across both x and y dimensions to ensure that the high wavenumbers in the Fourier spectrum of SSH remain consistent with the target Fourier spectrum.

$$\mu_x\left(t+\Delta t,\theta\right)=\frac{1}{M(K_{Nx}-K_{cx})}\sum_{m=1}^{m=M}\sum_{k=K_{cx}}^{k=K_{Nx}}\left|\widehat{\mathcal{F}}_x\left[\mathbf{X}\left(t+\Delta t\right)\right]-\widehat{\mathcal{F}}_x\left[\hat{\mathbf{X}}(t+\Delta t)\right]\right|_k. \tag{5a}$$

$$\mu_y\left(t+\Delta t,\theta\right)=\frac{1}{M(K_{Ny}-K_{cy})}\sum_{m=1}^{m=M}\sum_{k=K_{cy}}^{k=K_{Ny}}\left|\widehat{\mathcal{F}}_y\left[\mathbf{X}\left(t+\Delta t\right)\right]-\widehat{\mathcal{F}}_y\left[\hat{\mathbf{X}}(t+\Delta t)\right]\right|_k. \tag{5b}$$

$$\mu(t+\Delta t,\theta)=a\mu_x(t+\Delta t,\theta)+b\mu_y(t+\Delta t,\theta) \tag{6}$$

Here, M is the number of training samples (batch size), k represents a single Fourier mode, K_N is the highest Fourier mode present along the respective axis, K_c is the "cutoff" Fourier mode i.e. the minimum mode of interest, and $\widehat{\mathcal{F}}_x$ and $\widehat{\mathcal{F}}_y$ denote Fourier transforms along the zonal and meridional axis, respectively. Recall that $\hat{\mathbf{X}}(t)$ is the predicted SSH field at time t and $\mathbf{X}(t)$ is the SSH field given by the reanalysis at time t. After extensive trial and error, the best performance of OceanNet was observed with $K_{cx}=10$ and $K_{cy}=30$. Coefficients a and b are scaling factors used to ensure the order of magnitude of μ_x agrees with the order of magnitude of μ_y as well as the magnitude of the MSE loss (Eq. 7). Both a and b were determined via hyperparameter optimization to be 0.25. After combining our spectral loss function with the typical MSE loss, the full loss function for $t+\Delta t$ given by $\mathbf{L}\left(t+\Delta t,\theta\right)$ is:

$$\mathbf{L}_1\left(t+\Delta t,\theta\right)=\frac{1}{MN_o}\sum_{m=1}^{m=M}\sum_{n=1}^{n=N_o}\left(\mathbf{X}(t+\Delta t)-\hat{\mathbf{X}}(t+\Delta t)\right)_n^2 \tag{7}$$

$$\mathbf{L}\left(t+\Delta t,\theta\right)=(1-\lambda)\mathbf{L}_1(t+\Delta t,\theta)+\lambda\mu(t+\Delta t,\theta) \tag{8}$$

where $\mathbf{L}_1$ is MSE over N_o ocean grid points and λ is a weighting factor determined via hyperparameter optimization to be 0.2.

During single-time-step training, a weighted loss function of spectral regularization and MSE is used to constrain the model. To stabilize the model over multiple autoregressive predictions, the loss function is generalized to incorporate the sum of the loss function evaluated at each predictive step. The number of time steps over which the loss is calculated can be extended to any number of autoregressive steps; however, with each increase in the number of time steps the memory requirement for the subsequent backpropagation process during training grows exponentially thus the compromise of two timesteps was reached.

Architecture	Loss Function	Integration Scheme	RMSE (day 60)	MHD Saturation	CC=0
DLOP (U-NET)	MSE	None	0.24 m	40 days	60 days
DLOP (U-NET)	MSE	PEC	0.24 m	36 days	80 days
DLOP (U-NET)	MSE and SR	None	>1 m	12 days	16 days
DLOP (U-NET)	MSE and SR	PEC	>1 m	20 days	44 days
OceanNet (FNO)	MSE	None	0.28 m	>120 days	>120 days
OceanNet (FNO)	MSE	PEC	0.29 m	72 days	104 days
OceanNet (FNO)	MSE and SR	None	0.31 m	60 days	64 days
OceanNet (FNO)	MSE and SR	PEC	0.31 m	60 days	80 days

Table 1. Summary of experiments conducted. SR refers to "Spectral Regularization." "MHD saturation" refers to the day when the saturation value is reached. "CC=0" denotes the amount of time it takes the respective model to have a correlation coefficient value of 0. Metrics are explained in further detail below.

3   Results

This section presents a comparison of mesoscale ocean circulation dynamics represented by spatio-temporal evolution of SSH fields generated by various iterations of DLOP and OceanNet with the dynamical ROMS forecast using independent reanalysis data. To assess the performance rigorously, both qualitative and quantitative measures are employed. The metrics for evaluating predictive accuracy of SSH include RMSE and CC, which are widely recognized and employed in forecasting (Pathak et al., 2022; Bi et al., 2023a; Lam et al., 2023; Chattopadhyay and Hassanzadeh, 2023). In addition, a specialized object-tracking metric to evaluate the prediction of major ocean features delineated by SSH contours is incorporated: the modified Hausdorff distance (MHD,Dukhovskoy et al. (2015)). MHD quantifies the comparison of predicted objects to their counterparts between grids; identical shapes at identical locations yield an MHD of zero. To calculate MHD, at least one shape needs to be identified in each image. For the GSM, the contour identifying the northern frontal boundary of the meander was chosen to be used in MHD calculations. This boundary of the GSM is indicated by using a contouring threshold of SSH pertaining to the average SSH across all points in the reanalysis dataset with geostrophic speeds exceeding the average zonal maximum. This SSH contour is approximately -0.17m. While this defined northern boundary of the GSM is not illustrated by a contour line on most figures, an example of it can be seen in Fig. 1(b). The choice of this method for defining the GSM's position proves convenient since it provides a single object which is present in all images- if a contouring level which captures the shapes of individual eddies independent of the GSM where chosen, the calculation of the MHD score becomes tedious due to the possibility of having a mismatch in the number of objects between prediction and validation images. To provide a comprehensive assessment, qualitative snapshots of the predicted SSH fields generated by OceanNet, ROMS dynamical forecasts, and the independent SSH fields derived from the reanalysis are shown.

The ROMS forecasts used for comparison consists of 69 uncoupled 120-day predictions initialized five days apart. For fair comparison with the reanalysis dataset, the five-day mean SSH fields of the ROMS output were compared. Since OceanNet has no knowledge of the atmospheric states nor ocean boundary conditions during its inferencing, the ROMS forecasts were forced with persistent atmospheric and ocean boundary conditions for each run.

In regional ocean forecasting, defining surface and boundary forcing is a significant challenge, particularly when accurate and continuous global ocean and atmosphere forecasting data for extended periods is unavailable. Currently, almost all global ocean and atmosphere forecasts extend only 7-10 days, whereas our research requires forecasts with a duration of 120 days. None of the operational global models routinely provide such long-term forecasts. Persistence, in this context, refers to the assumption that future conditions will resemble past conditions. This approach can be used to define boundary and surface forcing for regional-scale models; however, it is important to understand the limitations of persistence and how it is applied in practice. Persistence is commonly used in short- to medium-term ocean forecasting due to its simplicity (e.g., Jacox et al. (2020)), but it does not account for changes in climatic conditions such as those driven by El Niño or other large-scale climate phenomena. While persistence can provide a baseline, it is not expected to capture full variability or trends in long-term forecasts. We acknowledge the limitation of using persistent forcing in driving ROMS forecasts. This limitation lies not with ROMS, as a dynamical model, but with the specific ROMS forecast configuration that we adopted in this study. An example of the 2 m air temperature and 10 m wind vectors used to initialize and force a single ROMS simulation is provided (Fig. 4).

A qualitative assessment reveals that OceanNet effectively captures the SSH propagation of undulations in the northern boundary of the GSM (Fig. 5). Moreover, OceanNet skillfully captures large-scale eddies traveling into and out of the domain, even without receiving any boundary information. In contrast, ROMS dynamical model forecast tends to overpredict SSH and the meridional amplitude of the northern boundary. While it is sensitive to initial conditions, OceanNet remains physically consistent over long-term forecasts in this region. Also, OceanNet provides stable and physically reasonable SSH predictions for the GSM for at least 120 days (not shown for brevity).

For quantitative comparisons, predictions from each model (OceanNet, ROMS) and persistence are compared to the reanalysis dataset to derive metrics at each day of prediction and are presented as averages of the nth day of prediction (Fig. 6). This method allows performance to be evaluated by forecast lead time across various initialization states; an evaluation of RMSE on the 20th day of prediction is an average measure of model performance with a forecast lead of 20 days given 69 different initial conditions. Each model was also compared to the saturation value of each metric: the 95th-percentile of the corresponding metric calculated from 1,000 random pairs of images from the entire reanalysis dataset (DelSole, 2004; DALCHER and KALNAY, 1987). If a metric exceeds the corresponding saturation value, the confidence in the prediction is considered to be no more trustworthy that that of selecting a random field of SSH from the reanalysis dataset. It is also important to note that not just the means of the ensembled metrics are investigated, but the corresponding standard deviations of each metric are also considered. If the means of two objects of comparison fall within the standard deviations of each other, not much weight can be put into claiming one model to perform better than the other. In these manners, OceanNet consistently outperforms ROMS in RMSE, CC, and MHD computed between the predicted SSH values and the reanalysis SSH over 120 days (Fig. 7). Persistence forecasting also fares reasonably well in this region due to the strong background state of the GSM; however,
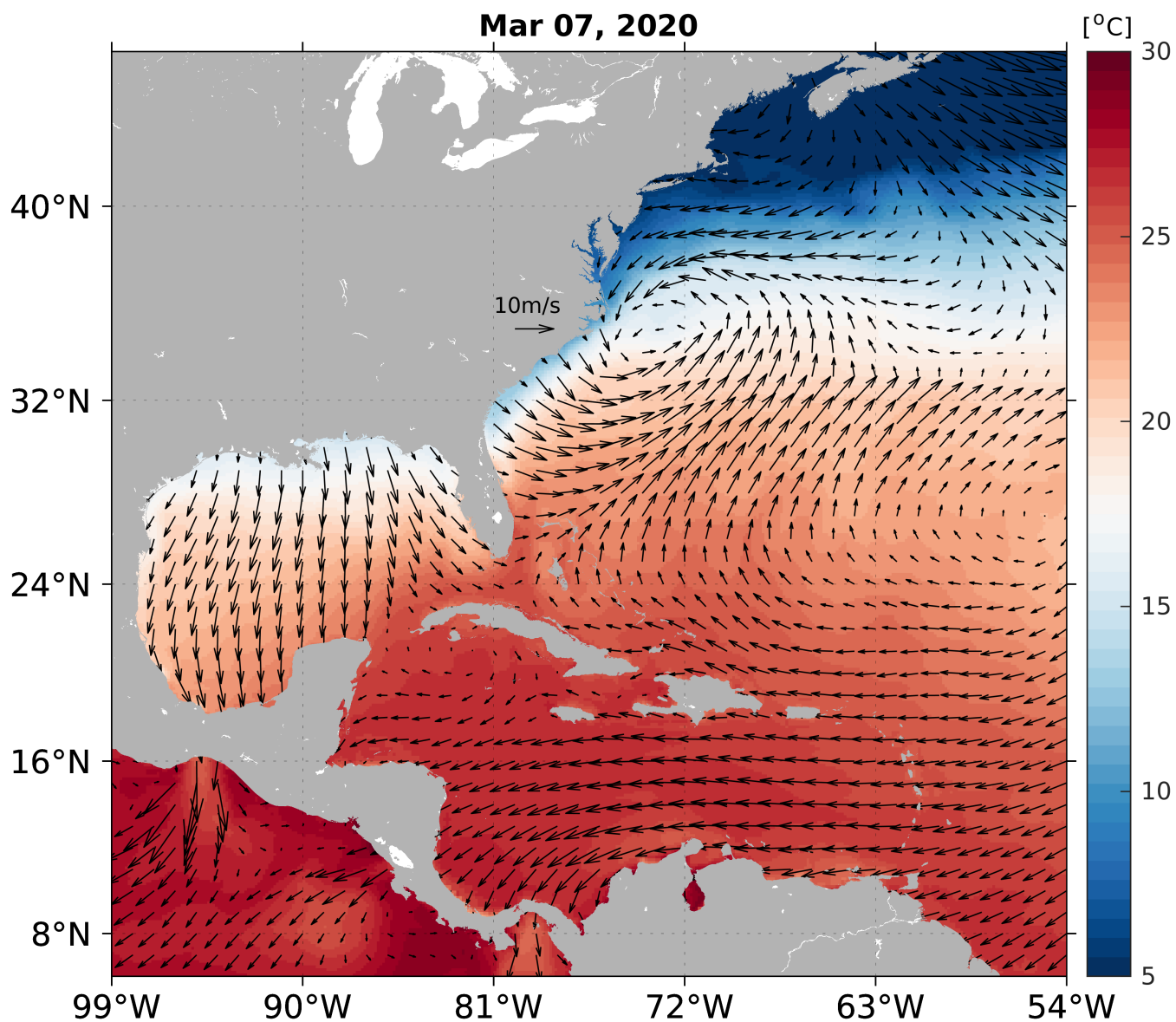
Figure 4. An example of atmospheric conditions used to force the uncoupled numerical simulations in ROMS- used in the simulation initialized on March 7th, 2020. Variables shown: 2 m air temperature (shading) and 10 m wind vectors (every eighth grid point plotted for visual clarity).
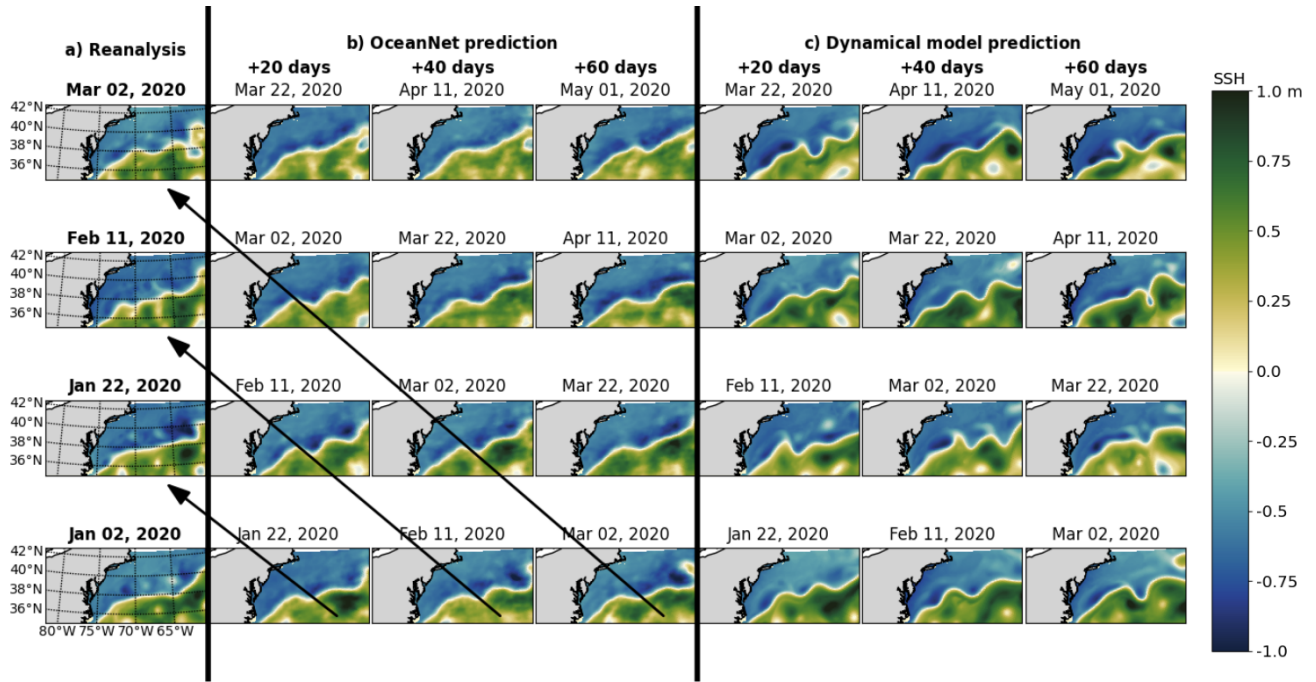
Figure 5. Performance of OceanNet for GS prediction. (a) SSH fields from the ocean reanalysis. (b) Predicted SSH generated by OceanNet. (c) ROMS dynamical model forecasts. In both OceanNet and dynamical model predictions, each row was initialized with the corresponding reanalysis data in the left column. SSH forecasts are provided for 20, 40, and 60 days. To evaluate the predictions, we can perform a diagonal comparison with the reanalysis SSH, as indicated by the black arrows in (b). The same diagonal comparison can also be conducted with the ocean reanalysis data for (c).

OceanNet can still outperforms persistence in all three metrics over 120 days on average. The MHD of OceanNet is shown to cross the saturation value of 62.34 km on day 60, suggesting the northern boundary of the GSM predicted by OceanNet is no better than selecting a random image from the reanalysis dataset. This is not to say that the position of the entire GSM is off, but that the undulations present in the GSM's northern boundary are completely out of phase. When this is the case, OceanNet does maintain the correct relative position of the GSM while ROMS frequently places the GSM too far north or south.

The RMSE, anomaly correlation coefficient (ACC), and MHD are compared across different iterations of the DLOP and FNO models, focusing on integration schemes and loss function terms. The two integration schemes compared were the absence of integration and PEC. The loss function terms compared were MSE and MSE with spectral regularization. This combination of model types, integration schemes, and loss function terms results in eight models to compare, following the same approach as before (ensembled metrics, Fig. 6), against each other and with ROMS and persistence predictions.

RMSE not only indicates the magnitude of values present but also serves as a measure of accuracy and stability. A high RMSE suggests that the magnitudes in the analyzed field are, on average, less realistic. If RMSE continues to increase over time, it implies that the model is becoming unstable. In terms of RMSE, the two DLOP models with spectral regularization
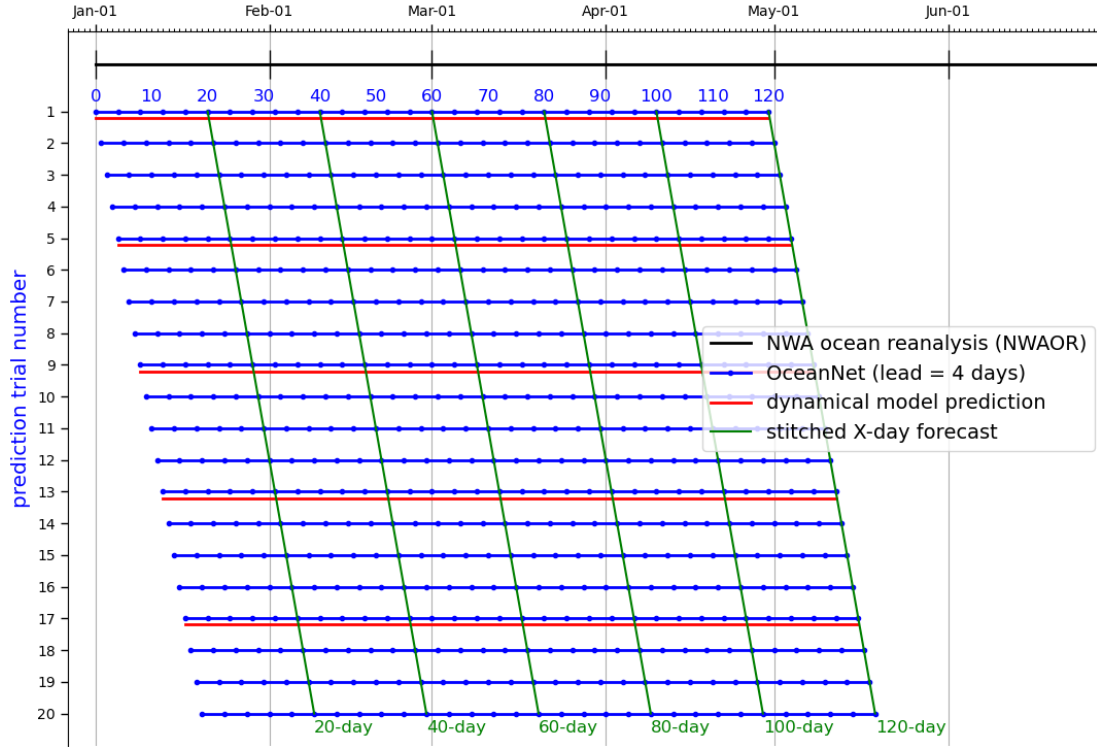
Figure 6. Visual explanation (example) of the ensembling of metrics for the evaluation of OceanNet across various ocean states. The explanation is framed with reference to OceanNet, but applies to the analysis of all iterations of DLOP and FNO models. The black line shows the time period covered by the reanalysis dataset with daily output. Blue lines represent individual OceanNet predictions trials spanning 120 days, each initialized one day apart, while blue dots indicate output timesteps of the model (every four days). Red lines represent individual ROMS predictions, which were initialized every five days with output given every day. Trials where the initialization dates between both ROMS and OceanNet align were compared qualitatively (visual comparison of output fields) along the green lines and quantitatively (RMSE, CC, and MHD) at all timesteps.
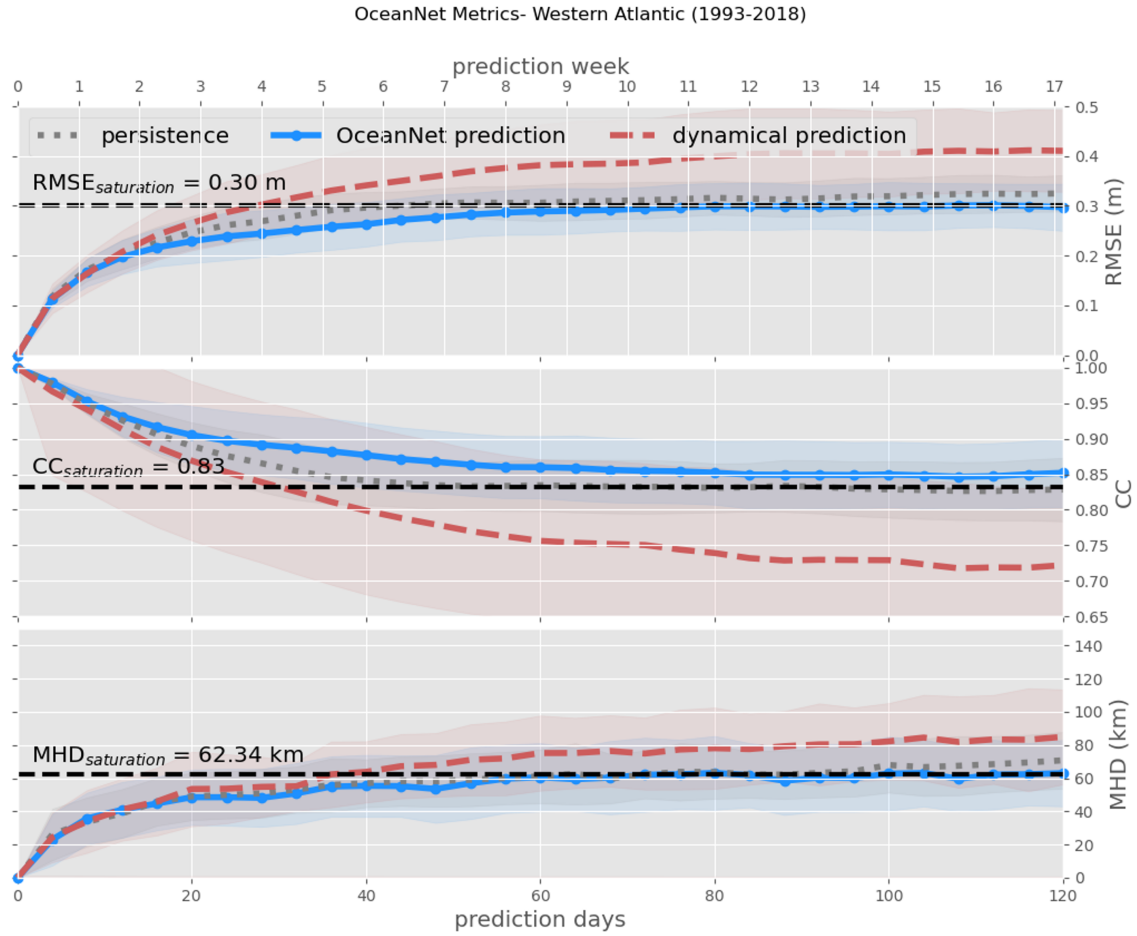
Figure 7. OceanNet's performance metrics in the northwest Atlantic: RMSE (top), CC (middle), and MHD (bottom), compared to the persistence forecast and ROMS dynamical model forecast. The performance statistics, calculated based on forecasts of 0-120 days, are displayed as mean values (lines) with standard deviations (shading). The black horizontal dashed lines denote saturation values, which are determined as 95% of the means derived from 1,000 pairs of random images in the reanalysis dataset. These representations illustrate how each method's statistics compare with the target SSH from the reanalysis dataset".
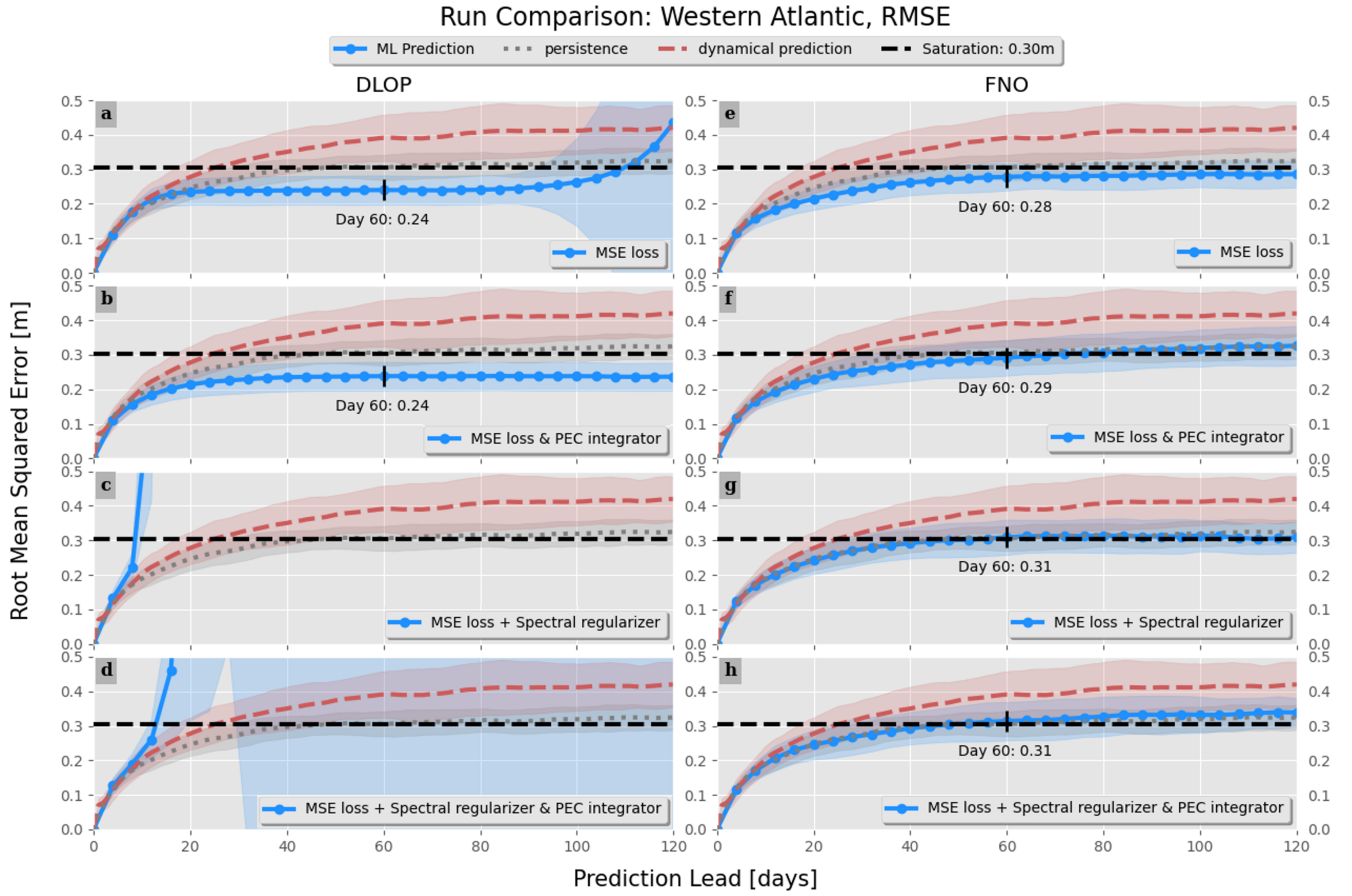
Figure 8. Comparison of RMSE between combinations of models, integration schemes, and loss function terms. Values with RMSE at day 60 are indicated. Line colors and styles are indicated by the legend and represent the mean value across all model runs. Shading represents the range of +/- 1 standard deviation. (a-d) DLOP models. (e-h) FNO models. (a,e) MSE loss function with no integration scheme. (b,f) MSE loss function with PEC integration. (c,g) MSE with spectral regularization and no integration scheme. (d,h) MSE with spectral regularization and PEC integration. Due to instabilities in the models, panes (c) and (d) had RMSE values of high enough magnitude to be unable to show in a meaningful plot.

305   included in the loss functions can immediately be identified as becoming unrealistic and unstable within a couple timesteps since they almost immediately cross the saturation threshold and continue to rise (Fig 8). The two DLOP models with only MSE in their loss function appear to perform well, especially when the PEC integrator is present, but the very basic DLOP model with MSE loss and no other augments does appear to become unstable around day 100. Out of all the DLOP models, the only one with competitive RMSE at all time steps is the iteration with PEC integration and MSE loss. For the FNO model,

310   all combinations of integration schemes and loss function terms are approximately the same; however, they all show slightly higher RMSE at day 60, that continues to increase in time, than the DLOP model with PEC integration and MSE loss.
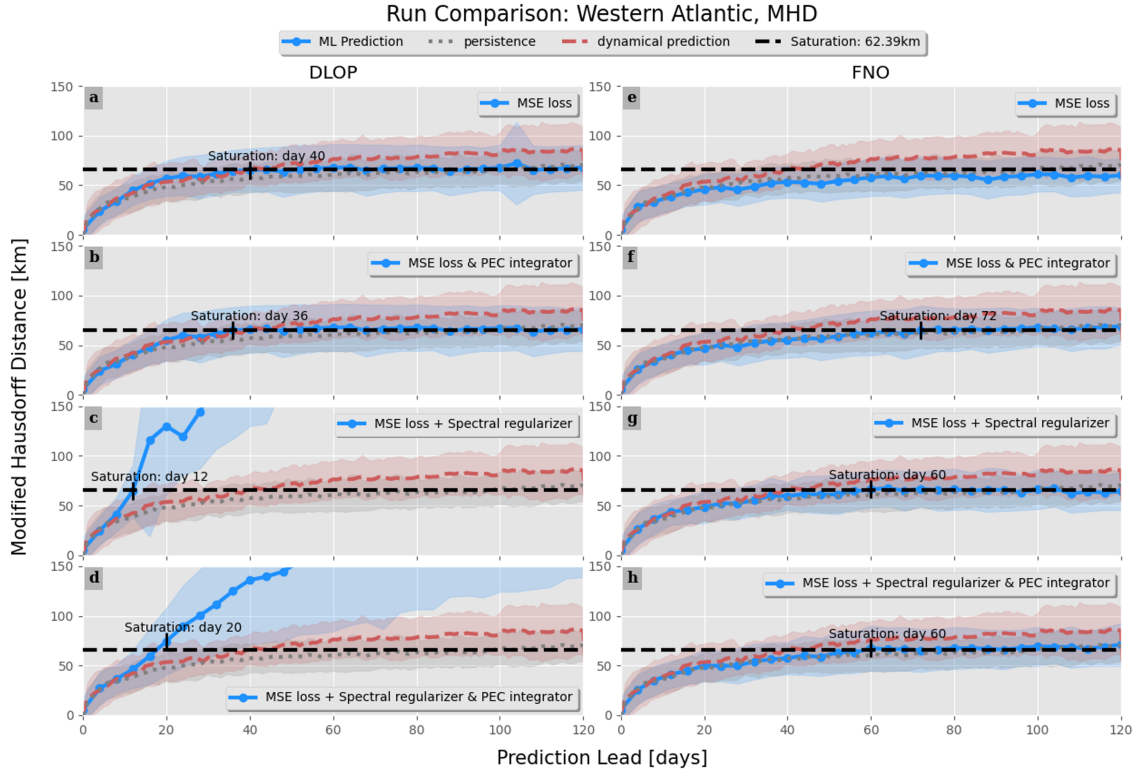
Figure 9. Same as Fig.8 but for MHD. The day at which each iteration of the models crosses the saturation value is indicated.

The plots regarding RMSE are a great initial impression of performance, but other metrics are important to consider when choosing the best model. That said, the MHD plots tell a similar story to RMSE, with the only differences to note being: DLOP with MSE loss does not become unstable in terms of MHD, and all the FNO models remain under the saturation value for longer than the two best DLOP models identified in the RMSE plots (Fig. 9). Taking the analyses of RMSE and MHD together, it seems as though the best model may be any of the FNOs or DLOP with MSE loss. The final metric investigated is the ACC. Like the CC, ACC is a comparison of how closely correlated two sets of data are, but ACC considers the field with the long-term pointwise mean removed prior to comparison. The removal of the long-term mean allows comparison of the two datasets on a finer scale. From the ACC, the results of the RMSE and MHD analyses are confirmed and the qualifying best models are selected to be any version of the FNO and the DLOP model with PEC integration and MSE loss since these models are at least competitive with the ROMS predictions across all timesteps in all three metrics (Fig. 10). This is the extent of the analysis possible from the provided metrics so to identify the absolute best model one must compare the actual fields of SSH predictions produced by each model to ensure they make physical sense.

While there are four versions of the FNO model which, metrically, appear to be competitive, extensive hyperparameter tuning and subsequent verification revealed the best of these to be the FNO with PEC integration and MSE loss with spectral
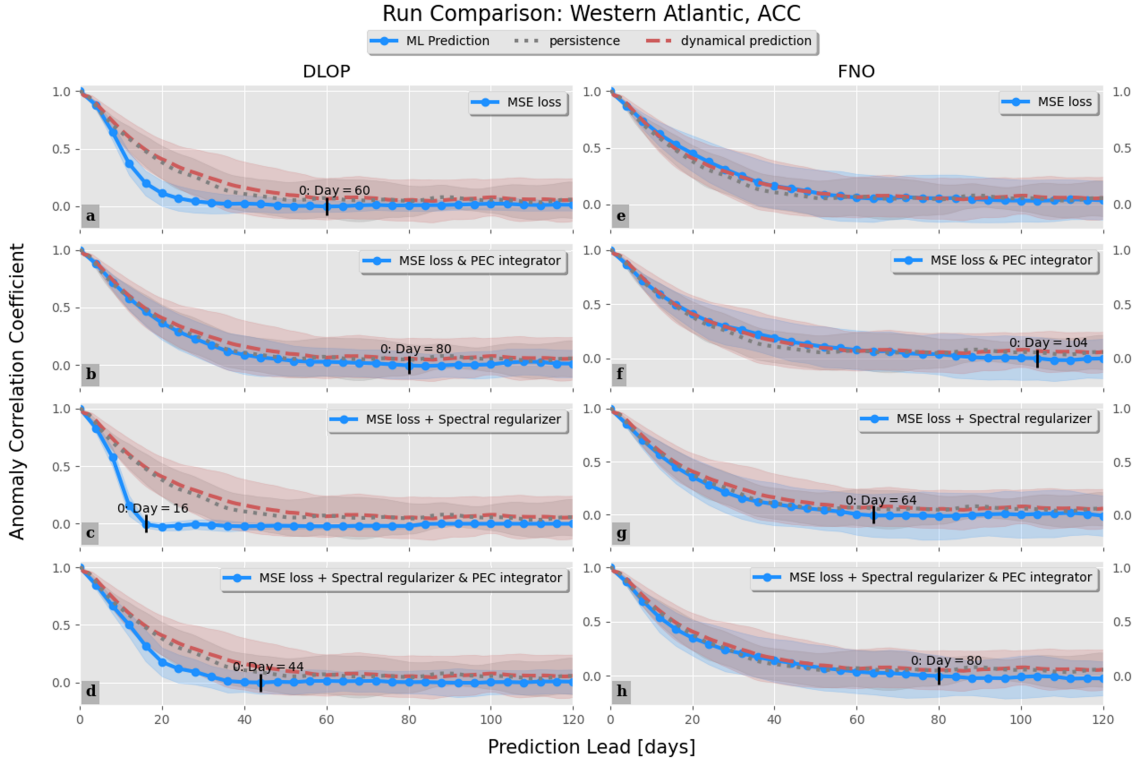
Figure 10. Same as Fig.8 but for ACC. The day at which each iteration of the models reaches a value of 0 is indicated.

regularization. This model, with the addition of the two-timestep loss described in Sect.2.5, became what is presented here as OceanNet. Covering the individual results of hyperparameter tuning each FNO model and presenting then comparing the verification of their physical fields is beyond the scopes of this paper. An example prediction of a single instance of prediction with a lead of 40 days made by the best DLOP model, ROMS, and the finalized OceanNet model is shown to demonstrate the difference between the physical fields predicted by each type of model (Fig. 11).

4 DISCUSSION & CONCLUSIONS

This study demonstrates the capabilities of the neural operator-based OceanNet: a data-driven machine learning model for GSM prediction over subseasonal-to-seasonal time scales. The techniques explained throughout Sect. 2.2 (FNO, PEC-integration, spectral regularization, and multi-timestep criterion) mitigate autoregressive error growth and the spectral-bias seen in other data-driven architectures, making OceanNet a solid candidate to function as a digital twin for long-term regional ocean circulation simulations.

Using high-resolution SSH data for the years 1993 through 2018, OceanNet was trained to predict ocean states with a four day lead time. The ability of OceanNet to autoregressively forecast the mesoscale ocean processes of the GSM over 60-120
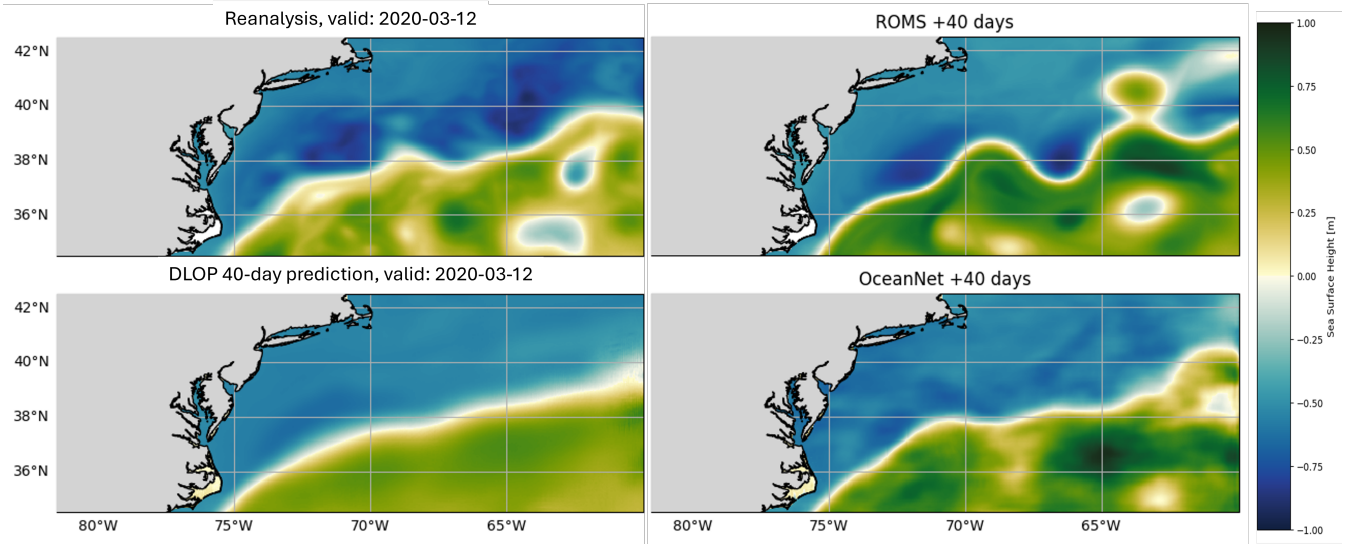
Figure 11. Prediction performance of a DLOP, ROMS, and OceanNet on the GSM region at 40 days. The SSH field 40 days after model initialization of 2020-02-01 described in Sect. 3, for (Top-left) the reanalysis dataset, (Top-right) ROMS, (Bottom-left) DLOP, and (Bottom-right) OceanNet.

days was evaluated by standard metrics used in machine learning and oceanographic communities. The results of this study provide two main conclusions: OceanNet remains remarkably stable over many iterations of autoregressive prediction and the model consistently outperforms ROMS dynamical forecasting across various initial ocean states in terms of RMSE, CC, and MHD. In addition, an inherit advantage of machine learning models in general are their ability to inference at tremendous speeds (4,000,000 times faster, in this case). These results demonstrate the potential of utilizing scientific machine learning to develop long-term stable, and accurate data-driven ocean models of great computational efficiency, paving the way for realizing a data-driven digital twin encompassing the entire climate system.

While the skill of OceanNet is impressive, the conclusions presented here are not without limitations. This study was conducted and trained on a single ocean feature, of a single spatial and temporal scale, from a reanalysis dataset utilizing only a single variable. Real-world ocean forecasting systems operate with full-physics dynamical ocean models and real-time observational ocean data, covering dynamic processes across diverse spatial and temporal scales. The disparities between these data sources and scales necessitate further investigation into OceanNet's performance across various ocean applications. The comparisons between OceanNet and ROMS can also be considered to have a major caveat: ROMS as a regional ocean model depends on persistent forcing conditions at open boundaries, for which persistent boundaries were provided in this study. While this method of modeling is operational in the sense that the absence of subseasonal-to-seasonal prediction often lacks forcing information on similar timescales thus persistence must be used, it may be more fair to compare the performance of OceanNet to a model which does not require boundary conditions, such as a global ocean model. The use of a global model would be expensive due to the resolution OceanNet uses, so perhaps the best comparison could be done once OceanNet is expanded to

cover the global ocean as well. Efforts to apply OceanNet to the global ocean are currently underway by our research team and will be reported in a future correspondence. In the meantime, the potential for OceanNet to include multiple state variables, such as surface currents, temperature, or even depth-averaged variables, could improve prediction of smaller scale circulations

360   and events, such as shelf break jets and frontal currents as well as provide more variables to compare to numerical methods. In addition, OceanNet produces very smooth, continuous fields which can potentially lead to an underestimation of the magnitudes of extreme ocean events; therefore, additional research is imperative to assess OceanNet's performance under extreme ocean conditions, e.g., during severe storms.

Significant opportunities exist for improvement in both AI-based methods and dynamical model-based ocean forecasting.

365   In the AI domain, potential advancements involve the integration of subsurface ocean states and additional ocean variables, the incorporation of temporal dimensions through the training of four-dimensional deep networks, and the exploration of more complex network architectures with increased depth and breadth. In the realm of numerical ocean forecast modeling, the development of pre- and post-processing techniques can help mitigate the inherent biases found in ocean models. We expect that a hybrid approach, combining data-driven and dynamical numerical models will play a pivotal role in pushing the

370   boundaries of excellence in ocean prediction.

Code and data availability.   The codes used in this study are openly available at https://github.com/magray-ncsu/OceanNet. Data used in this study is available upon request.

Author contributions.   All authors contributed equally to the research conducted and the writing of the paper.

Competing interests.   None of the authors declare any competing interests.

375   *Acknowledgements.*   We thank Subhashis Hazarika and Maria Molina for the insightful discussions, Jennifer Warrillow for editorial assistance, and Elisabeth Brown and Gary Lackmann for their rigorous critiques of this manuscript. M. Gray, A. Lowe, T. Wu, and R. He, were supported by NSF awards 2019758 and 2331908. A. Chattopadhyay performed partial work at the Palo Alto Research Center, SRI International.

References

380   Agarwal, N., Kondrashov, D., Dueben, P., Ryzhov, E., and Berloff, P.: A Comparison of Data-Driven Approaches to Build Low-Dimensional Ocean Models, Journal of Advances in Modeling Earth Systems, 13, e2021MS002 537, 2021.

Bi, K., Xie, L., Zhang, H., Chen, X., Gu, X., and Tian, Q.: Accurate medium-range global weather forecasting with 3D neural networks, Nature, pp. 1–6, 2023a.

Bi, K., Xie, L., Zhang, H., Chen, X., Gu, X., and Tian, Q.: Accurate medium-range global weather forecasting with 3D neural networks,
385   Nature, 619, 533–538, https://doi.org/10.1038/s41586-023-06185-3, 2023b.

Chassignet, E. and Marshall, D.: Gulf Stream separation in numerical ocean models, American Geophysical Union, 2008.

Chassignet, E. P. and Xu, X.: Impact of Horizontal Resolution (1/12° to 1/50°) on Gulf Stream Separation, Penetration, and Variability, Journal of Physical Oceanography, 47, 1999–2021, https://doi.org/10.1175/jpo-d-17-0031.1, 2017.

Chattopadhyay, A. and Hassanzadeh, P.: Long-term instabilities of deep learning-based digital twins of the climate system: The cause and a
390   solution, arXiv preprint arXiv:2304.07029, 2023.

Chen, K., He, R., Powell, B. S., Gawarkiewicz, G. G., Moore, A. M., and Arango, H. G.: Data assimilative modeling investigation of Gulf Stream Warm Core Ring interaction with continental shelf and slope circulation, Journal of Geophysical Research: Oceans, 119, 5968–5991, https://doi.org/10.1002/2014jc009898, 2014.

Chttopadhyay, A., Gray, M. A., Wu, T., Lowe, A. B., and He, R.: OceanNet: A principled neural operator-based digital twin for regional
395   oceans, arXiv, p. 2310.00813, 2023.

DALCHER, A. and KALNAY, E.: Error growth and predictability in operational ECMWF forecasts, Tellus A, 39A, 474–491, https://doi.org/10.1111/j.1600-0870.1987.tb00322.x, 1987.

DelSole, T.: Predictability and Information Theory. Part I: Measures of Predictability, Journal of the Atmospheric Sciences, 61, 2425–2440, https://doi.org/10.1175/1520-0469(2004)061<2425:paitpi>2.0.co;2, 2004.

400   Dukhovskoy, D. S., Ubnoske, J., Blanchard-Wrigglesworth, E., Hiester, H. R., and Proshutinsky, A.: Skill metrics for evaluation and comparison of sea ice models, Journal of Geophysical Research: Oceans, 120, 5910–5931, 2015.

He, R., Wu, T., Mao, S., Zong, H., Zambon, J., Warrillow, J., Dorton, J., and Hernandez, D.: A high-resolution ocean reanalysis of the Northwestern Atlantic in 1993-2022, in prep.

Jacox, M. G., Alexander, M. A., Siedlecki, S., Chen, K., Kwon, Y.-O., Brodie, S., Ortiz, I., Tommasi, D., Widlansky, M. J., Barrie, D.,
405   Capotondi, A., Cheng, W., Lorenzo, E. D., Edwards, C., Fiechter, J., Fratantoni, P., Hazen, E. L., Hermann, A. J., Kumar, A., Miller, A. J., Pirhalla, D., Buil, M. P., Ray, S., Sheridan, S. C., Subramanian, A., Thompson, P., Thorne, L., Annamalai, H., Aydin, K., Bograd, S. J., Griffis, R. B., Kearney, K., Kim, H., Mariotti, A., Merrifield, M., and Rykaczewski, R.: Seasonal-to-interannual prediction of North American coastal marine ecosystems: Forecast methods, mechanisms of predictability, and priority developments, Progress in Oceanography, 183, https://doi.org/10.1016/j.pocean.2020.102307, 2020.

410   Krishnapriyan, A. S., Queiruga, A. F., Erichson, N. B., and Mahoney, M. W.: Learning continuous models for continuous physics, arXiv preprint arXiv:2202.08494, 2022.

Lam, R., Sanchez-Gonzalez, A., Willson, M., Wirnsberger, P., Fortunato, M., Alet, F., Ravuri, S., Ewalds, T., Eaton-Rosen, Z., Hu, W., Merose, A., Hoyer, S., Holland, G., Vinyals, O., Stott, J., Pritzel, A., Mohamed, S., and Battaglia, P.: Learning skillful medium-range global weather forecasting, Science, 382, 1416–1421, https://doi.org/10.1126/science.adi2336, 2023.

415   Li, Z., Kovachki, N., Azizzadenesheli, K., Liu, B., Bhattacharya, K., Stuart, A., and Anandkumar, A.: Fourier neural operator for parametric partial differential equations, arXiv preprint arXiv:2010.08895, 2020.

Lowe, A. B., Gray, M. A., Wu, T., Chttopadhyay, A., and He, R.: Long-term predictions of Loop Current Eddy evolutions using a Fourier neural operator-based data-driven ocean emulator, Artificial Intelligence for the Earth Systems, 2024.

Minobe, S., Kuwano-Yoshida, A., Komori, N., Xie, S.-P., and Small, R. J.: Influence of the Gulf Stream on the troposphere, Nature, 452,
420   206–209, https://doi.org/10.1038/nature06690, 2008.

Pathak, J., Subramanian, S., Harrington, P., Raja, S., Chattopadhyay, A., Mardani, M., Kurth, T., Hall, D., Li, Z., Azizzadenesheli, K., et al.: FourCastNet: A global data-driven high-resolution weather model using adaptive Fourier neural operators, arXiv preprint arXiv:2202.11214, 2022.

Robinson, A. R., Spall, M. A., and Pinardi, N.: Gulf Stream Simulations and the Dynamics of Ring and Meander Processes, Journal of
425   Physical Oceanography, 18, 1811–1854, https://doi.org/10.1175/1520-0485(1988)018<1811:gssatd>2.0.co;2, 1988.

Wang, J. L., Zhuang, H., Chérubin, L. M., Ibrahim, A. K., and Ali, A. M.: Medium-Term Forecasting of Loop Current Eddy Cameron and Eddy Darwin Formation in the Gulf of Mexico With a Divide-and-Conquer Machine Learning Approach, Journal of Geophysical Research: Oceans, 124, 5586–5606, https://doi.org/10.1029/2019jc015172, 2019.

Wang, X., Wang, R., Hu, N., Wang, P., Huo, P., Wang, G., Wang, H., Wang, S., Zhu, J., Xu, J., Yin, J., Bao, S., Luo, C., Zu, Z., Han, Y., Zhang,
430   W., Ren, K., Deng, K., and Song, J.: XiHe: A Data-Driven Model for Global Ocean Eddy-Resolving Forecasting, arXiv, p. 2402.02995v2, 2024.

Weyn, J. A., Durran, D. R., and Caruana, R.: Can Machines Learn to Predict Weather? Using Deep Learning to Predict Gridded 500-hPa Geopotential Height From Historical Weather Data, Journal of Advances in Modeling Earth Systems, 11, 2680–2693, https://doi.org/10.1029/2019ms001705, 2019.

435   Wu, T. and He, R.: Marine Heatwaves in the Deep-Sea Benthic Ecosystems of Northwest Atlantic Continental Margin, in prep.

Xu, Z.-Q. J., Zhang, Y., Luo, T., Xiao, Y., and Ma, Z.: Frequency principle: Fourier analysis sheds light on deep neural networks, arXiv preprint arXiv:1901.06523, 2019.

Zeng, X., Li, Y., and He, R.: Predictability of the loop current variation and eddy shedding process in the Gulf of Mexico using an artificial neural network approach, Journal of Atmospheric and Oceanic Technology, 32, 1098–1111, 2015.